PHYSICAL REVIEW B **89**, 144202 (2014)

Quantitative modeling of solute drag by vacancies in face-centered-cubic alloys

Thomas Garnier,[1,2,*] Dallas R. Trinkle,[2] Maylise Nastar,[1] and Pascal Bellon[2]
[1] *CEA, DEN, Service de Recherches de Métallurgie Physique, F-91191 Gif-sur-Yvette, France*
[2] *Department of Materials Science and Engineering, University of Illinois at Urbana-Champaign, Urbana, Illinois 61801, USA*

(Received 20 December 2013; published 17 April 2014)

Transport coefficients, the elements of the so-called Onsager matrix, are essential quantities for modeling solid-state kinetics controlled by diffusion. In a face-centered-cubic structure, drag of solute atoms by vacancies can be caused by solute-vacancy binding at nearest neighbors. In order to investigate solute drag in alloys with interactions up to the third-nearest-neighbor sites, we extend an analytic method: the self-consistent mean field method. With this method, we calculate the Onsager matrix of model alloys to identify kinetic effects arising from individual and collective jump frequencies and assess the results on select cases using atomic kinetic Monte Carlo simulations. Using preexisting density functional theory data from various sources, we show that many impurities have low-temperature solute drag before changing to solute exchange at high temperatures. We evaluate the transition temperature for these alloys between these two regimes and compare the results with available experimental data. Some disagreement is found, which can be due both to experimental and numerical shortcomings. In order to guide diffusion calculations, the sensitivity of the Onsager matrix to the range of the kinetic correlation and to the input density functional theory data is studied.

DOI: 10.1103/PhysRevB.89.144202 PACS number(s): 61.82.Bg, 66.30.Fq, 72.15.−v

Usually, a specific microstructure is required to obtain an alloy with outstanding mechanical properties. Controlling the microstructure requires knowledge of atomic diffusion in different situations, as atomic transport drives phenomena such as the chemical homogenization during casting [1,2] or the rate of precipitation of secondary phases during heat treatment [3,4]. An important case is that of alloys under irradiation where point defects are created in the bulk of the material. These defects enhance diffusion [5], but also induce new phenomena such as the creation of dynamical microstructure [6] or the solute segregation and precipitation at microstructural elements like dislocations, grain boundaries, and surfaces [7–9]. This segregation is due to a kinetic coupling between the point defect fluxes and the atomic species present in the alloy. In austenitic steels, radiation-induced segregation leads to a chromium depletion at grain boundaries under irradiation, which could affect corrosion resistance [9–12]. Flux coupling can even lead to the nucleation of thermodynamically unstable phases like Ni_3Si in the case of undersaturated Ni(Si) alloys under irradiation [8,13].

In a near-equilibrium system, the atomic flux per unit area J^α of a chemical species α is related to the gradients of chemical potential $\nabla\mu^\beta$ of all atomic species β by the Onsager matrix $L_{\alpha\beta}$:

$$\vec{J}^\alpha = -\sum_\beta L_{\alpha\beta}\vec{\nabla}\left(\frac{\mu^\beta}{k_B T}\right), \tag{1}$$

where k_B stands for the Boltzmann constant and T for the temperature. The Onsager matrix thus describes the flux coupling and its calculation can predict radiation-induced segregation [11]. The Onsager matrix is also required for accurate mesoscopic kinetic simulations such as the phase field approach [14–16]. However, in most cases only simplified models are being used for the description of kinetic properties; for example, in DICTRA only the diagonal terms of the Onsager matrix are considered [17]. These approximations limit the possibilities for these models to provide quantitative predictions, as they miss qualitative effects induced by correlations terms in the Onsager matrix like solute drag by vacancies. In particular, in the presence of a gradient of chemical potential of vacancies, solute atoms can diffuse even if the chemical potential of solute is spatially uniform. This phenomenon is due to the off-diagonal terms in the Onsager matrix that are induced by kinetic correlations, and was observed experimentally in quenched dilute alloys [18–20]. This effect of a flux of vacancies on atomic diffusion is called the inverse Kirkendall effect [21,22]. If a sufficiently stable solute-vacancy complex is formed, the vacancy will drag the solute during its migration [23], leading to solute segregation near a vacancy sink. If, instead, the complex quickly dissociates, then solute drag does not occur but the inverse Kirkendall effect remains and site conservation results in a flux of atoms in the opposite direction of the vacancies to fill the empty spaces. If solute atoms diffuse faster than matrix, the net result is a depletion of solute atom near the vacancy sink. In the opposite case, with matrix atoms that diffuse faster, solute atoms segregate near a vacancy sink, even without solute drag.

The crystal structure plays an important role in the onset of solute drag. Consider a dilute alloy on a face-centered-cubic (fcc) lattice, which is the focus of this work. The vacancy can move around the solute from one first-nearest-neighbor (NN) site of the solute to another, without breaking the solute-vacancy complex. If the frequency for the vacancy to move around the solute is larger than the frequency of dissociation of the complex, the vacancy will stay on an orbit of first-NN sites around the solute atom (which we will refer to as “1” orbit) long enough to drag the impurities [24]. However, other mechanisms can also induce solute drag. In a recent work [25], it has been shown that solute drag by vacancies could take place in an alloy on a body-centered-cubic (bcc) lattice with solute-vacancy binding energy limited to the nearest-neighbor sites. In this case and in contrast to the fcc lattice, the vacancy

---

[*] tgarnier@illinois.edu

©2014 American Physical Society

can not remain on first-NN sites of the solute when it diffuses by exchanging position with solvent atoms. Nonetheless, the vacancy can induce solute drag by alternating dissociation and association jumps around the solute. Moreover, as shown in Ref. [25], solute drag can also be caused by the trapping of the vacancy in the neighborhood of the solute, or by following other orbits when solute-vacancy interactions are important at larger distances.

First-principles thermodynamics have been very successful in predicting the equilibrium structure and properties of materials, and a growing effort is being done to obtain similarly kinetic properties of alloys by computing the frequencies of atomic jumps [2,4,26–34]. Density functional theory (DFT) results can then be coupled with analytic models [31–36] or atomic kinetic Monte Carlo (AKMC) simulations [26,29,30,37] to compute the Onsager matrix. Analytic methods are extremely computationally efficient since only a single matrix inversion is required to obtain the Onsager matrix [24]. As a consequence, they served as a guide to define the frequencies to compute in a number of cases [33,36]. In practice, these methods require a truncation of the solute-vacancy interactions. The first calculations for the fcc structure were performed within the five-frequency model where interactions are limited to the first-NN sites [38,39]. In the most advanced case, second-NN interactions have been only partially taken into account [40]. Moreover, a truncation of the kinetic correlations is required, and has an important effect in the case of alloys on a bcc lattice [25]. While AKMC simulations are not limited by the number of frequencies considered (cf. Ref. [24] and references therein), when complex atomic interactions or strong kinetic correlations are involved, as in the case of solute drag, the computational cost of AKMC simulations can make their use impractical. As the accuracy of the results provided by DFT calculations comes at the cost of ever more complex interatomic interactions, analytic methods remain desirable for efficient predictions and for error estimation and propagation.

Similar to the work performed for bcc alloys [25], the aim of this work is to understand the atomic scale origin of vacancy-induced drag effect in fcc alloys. For that purpose, systematic calculations of the Onsager matrix are required, including for systems with strong kinetic correlations. In order to overcome the limitations discussed in the previous paragraph, and gain physical insight, we rely on an analytic method to efficiently and systematically compute the Onsager matrix: the self-consistent mean field method (SCMF) [25,41]. An analytic model describes diffusion in fcc alloys with interactions up to the third-nearest-neighbor sites. We calculate all the coefficients (L_{ij}) of the Onsager matrix and identify solute drag with the drag ratio L_{BV}/L_{BB}, where B designates the solute atom and V the vacancy to identify solute drag [42]. L_{BB} is proportional to the tracer diffusion coefficient and is always positive while L_{BV} is positive when the solute atoms are dragged by the vacancies, and negative otherwise. As a consequence, the sign of the drag ratio is determined by L_{BV}, which measures the correlation in the diffusion of solute atoms and vacancies, and L_{BB} serves as a scaling factor. In the dilute limit, the drag ratio is independent of the vacancy and solute concentration.

We first briefly recall the general nomenclature for vacancy-atom exchanges and the results of the SCMF approach. We analytically calculate the Onsager matrix in a fcc alloy with solute-vacancy interactions up to third-NN sites that can be described by a set of 16 different frequencies. Next, we investigate the conditions for solute drag using AKMC simulations on select cases for verifying SCMF results. We determined the effect of each atomic frequency independently in the case of an ideal model alloy, and some collective effects are explored to identify the phenomena at the origin of solute drag by the vacancy. Finally, using DFT data from the literature, we identify the onset of solute drag for several Al-based, Ni-based, and UC-based fcc alloys and comment on the reliability of the results.

I. ANALYTIC CALCULATIONS OF THE ONSAGER MATRIX BY THE SCMF METHOD

We consider an alloy represented by a system of interacting atoms and vacancies distributed on a rigid lattice, where consecutive atomic jumps are considered to be independent random events, with stationary probability. In the case of a binary dilute alloy, where we consider vacancy-mediated kinetic events only, each transition from one configuration to another is due to the jump of an atom from an atomic site into the vacancy. Using the three-index notation defined in Ref. [25] for dilute alloys, the transition frequency between two configurations can be written $w_{abc}^{(\zeta)}$, where each index defines the relationship between two sites: a is the distance (in nearest-neighbor distances) from the site of the jumping atom to the vacancy site, b the distance from the site of the jumping atom to the solute site, and c the distance from the site of the solute to the vacancy site (see Fig. 1). As a consequence, b designates the vacancy-solute distance after the jump, while c is the distance before the jump. Moreover, for any distance beyond the solute-vacancy interaction range, the value ∞ is assigned to the index, as the numerical value is no longer relevant. The type of jump is identified with an index ζ corresponding to the five-frequency notation illustrated in Fig. 2: $\zeta = 2$ for a jump of the solute atom, $\zeta = 0$ for a jump of a matrix atom without any solute in interaction range, $\zeta = 1$ for a jump between two sites interacting with the solute, $\zeta = 3$ for a dissociative jump leading to a configuration where the solute atom is outside the interaction range, and $\zeta = 4$ for an

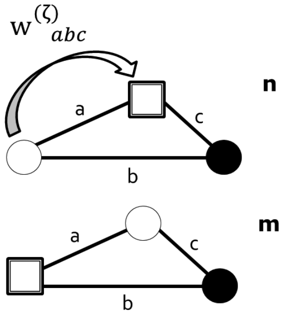

FIG. 1. Schematic of a vacancy jump in a dilute alloy in the initial configuration **n** (top) and final configuration **m** (bottom). The full circles represent the solute atom, the open circles a matrix atom, and the squares a vacancy, while a,b,c describe the distances between each species.

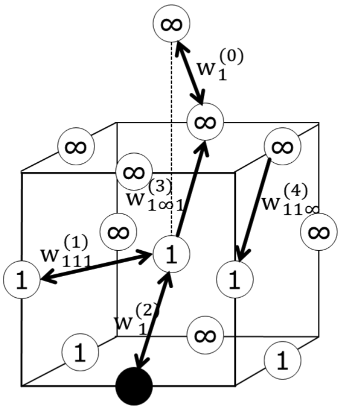

FIG. 2. Vacancy jump frequencies in a dilute fcc binary alloy with first-nearest-neighbor interactions. Arrows indicate the direction of the jumps. The solute atom is represented by a filled circle, and the numbers on lattice sites indicate the distance from the solute atom site, while an ∞ indicates sites beyond the range of the interactions.

associative jump leading to a configuration where the solute atom is inside the interaction range.

The SCMF method was developed initially for computing the Onsager matrix in vacancy-mediated diffusion in regular solid solutions (corresponding to a mean field Bragg-Williams approximation in alloys) [41] and later improved to take into consideration pair correlations [43]. A detailed description of the SCMF method can be found in Ref. [25]. A SCMF calculation is based on an atomic diffusion model related to the maximum range of the solute-vacancy interactions. Once this range is defined, the use of the SCMF method involves performing a single approximation: beyond a given distance, kinetic correlations are neglected. Considering interactions up to the first-nearest-neighbor sites, in the most simple calculations (usually called first shell approximation, here denoted 1NN), the kinetic correlations are neglected beyond the first-nearest-neighbor sites [38]. In a more refined calculation called second shell approximation, all the nearest-neighbor sites of these 12 sites are also included in the calculation of the kinetic correlation. SCMF calculations have been previously run in this approximation, here denoted 1NN1NN [43], which produces good agreement with other analytic methods [24]. In order to study the effect of the truncation of kinetic correlations, we performed more extended calculations. Extra shells were iteratively added for this purpose, increasing the number of sites involved by adding the ensemble of sites that can be reached by one jump starting from any site of the previous shell, resulting in a series of approximations $1\text{NN}(1\text{NN})^k$, where k takes an integer value.

In this work, in order to study alloys with solute vacancy interactions up to the third-nearest-neighbor sites, SCMF calculations were performed considering all the sites up to the third-nearest neighbors of the third-nearest-neighbor sites of the solute atom. Analytic results for this approximation, called 3NN3NN approximation, are given in the Appendix, and a routine is provided in the Supplemental Material [44] to reproduce the results obtained within this approximation and extending them to other alloys as input data become available. As this approximation is designed to handle systems with third-nearest-neighbor interactions, it is also able to provide results for systems with shorter-range interactions.

II. DRAG EFFECT MECHANISM IN THE FIVE-FREQUENCY MODEL

The reference five-frequency model is designed to describe alloys on a fcc lattice with vacancy-solute binding energy limited to first-NN sites. Using SCMF calculations in the 3NN3NN approximation, the onset of solute drag in an alloy described by this model is investigated. The terms of the Onsager matrix are nonlinear functions of the different frequencies. However, the drag ratio L_{BV}/L_{BB} describes the relative diffusion speed of the pair solute vacancy with respect to the diffusion of solute atoms, and so depends only on the ratios of the frequencies with $w_1^{(0)}$. Moreover, as solute-vacancy exchanges do not change the barycenter of the pair, the corresponding frequency $w_1^{(2)}$ does not impact the drag ratio. Finally, detailed balance determines the value of the ratio of two variables $w_{11\infty}^{(4)}$ and $w_{1\infty1}^{(3)}$ from the solute-vacancy binding energy.

We define an ideal model alloy as a solution in which solute-vacancy binding energies are null at all distances (zero heat of mixing), but in which the solute still disturbs the jump frequencies in its neighborhood. In this case, due to detailed balance $w_{11\infty}^{(4)} = w_{1\infty1}^{(3)}$. Thus, the drag ratio of an ideal model alloy described by the five-frequency model depends only on two different parameters: $w_{11\infty}^{(4)}/w_1^{(0)}$ and $w_{111}^{(1)}/w_1^{(0)}$. In Fig. 3, the value of the drag ratio computed using the SCMF method is represented as a function of $w_{11\infty}^{(4)}/w_1^{(0)}$, in the 1NN, 1NN1NN, and 3NN3NN approximations for a model alloy with $w_{111}^{(1)}/w_1^{(0)} = 1$. In order to validate the SCMF results and the choice of the kinetic approximation, atomic kinetic Monte Carlo simulations are performed to compute Onsager matrices using atomic jump frequencies identical to those used in SCMF calculations. AKMC simulations were performed

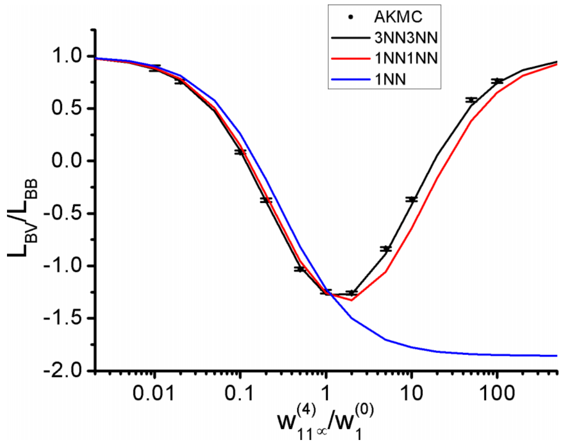

FIG. 3. (Color online) L_{BV}/L_{BB} ratio in a dilute fcc binary alloy described by the five-frequency model as a function of the ratio $w_{11\infty}^{(4)}/w_1^{(0)}$. Points represent the results of AKMC simulations, while the continuous (resp. dotted and dashed) lines represent SCMF calculations in the 3NN3NN (resp. 1NN and 1NN1NN) approximation. Error bars represent the statistic variance of the AKMC results.

using a 4×10^3 site simulation box containing a single solute atom and a single vacancy. The initial configuration is obtained by choosing random locations for the vacancy and the solute atom, and equilibrating the system for 10 Monte Carlo steps (MCS) ($1\text{MCS} = 2 \times 12^3$ vacancyjumps). Displacements of the atoms are recorded during 10MCS and the values averaged over 10^6 simulations. The Onsager matrix is obtained using the Kubo-Green formula [45,46]

$$L_{\alpha\beta} = c_v \left\langle \frac{R^\alpha R^\beta}{6V\tau} \right\rangle, \tag{2}$$

where c_v is the vacancy concentration, V is the atomic volume, and R^α the total displacement of all atoms of type α during the integration time τ. As a single vacancy is present in the simulation box, the Onsager matrix thus obtained corresponds to the dilute limit in vacancy concentration, even though the nominal concentration might be high. As in the dilute limit the Onsager matrix is a linear function of the vacancy concentration, the Onsager matrix of a system with a more realistic vacancy concentration can be obtained by replacing the nominal vacancy concentration with the desired vacancy concentration. The AKMC simulations show that the 1NN approximation fails to predict the qualitative kinetic behavior of the model alloy, as in the 1NN approximation L_{BV} remains negative for any value of $w^{(4)}_{11\infty}/w^{(0)}_1 > 1$. In comparison, the 1NN1NN approximation predicts the frequency at which this change of sign of L_{BV} occurs with a relative accuracy of 50%, while the 3NN3NN predicts this value within 5%.

Figure 4 provides a complete picture of the onset of solute drag as a function of both $w^{(4)}_{11\infty}/w^{(0)}_1$ and $w^{(1)}_{111}/w^{(0)}_1$, in the case of an ideal model alloy described by the five-frequency model. It can be observed that solute drag occurs either when $w^{(4)}_{11\infty}/w^{(0)}_1 \gtrsim 20$ or when $w^{(1)}_{111}/w^{(4)}_{11\infty} \gtrsim 10$. The first case corresponds to a vacancy turning around the solute atom by alternating dissociative and associative jumps. This situation is similar to what happens in the bcc structure described by the four-frequency model [25], where this movement has been called "1+" orbit. In the second case, $w^{(1)}_{111}/w^{(4)}_{11\infty} \gtrsim 10$ means that the vacancy turns around the solute from a nearest-neighbor site to another faster than it can escape from the solute and return to the bulk. The vacancy is thus trapped near the solute, which also occurs in the bcc structure, but only when interactions extend beyond first-NN sites [25]. As a ratio of 10 between two frequencies corresponds to a difference of migration barriers of the order of 50 meV at room temperature, vacancy trapping by the solute can be reasonably expected in real alloys.

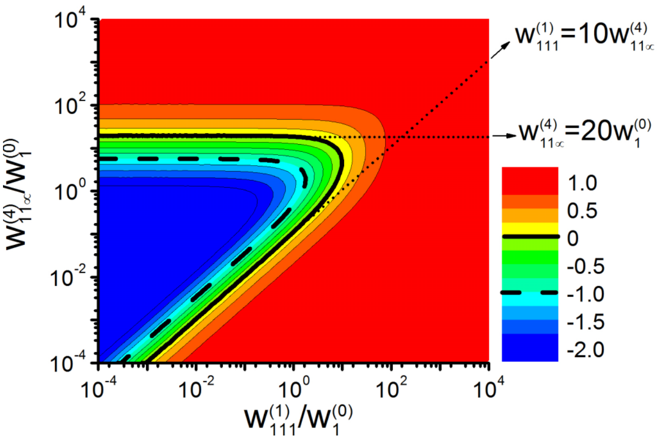

FIG. 4. (Color online) Contour map of L_{BV}/L_{BB} as a function of the ratios of frequencies $w^{(1)}_{111}/w^{(0)}_1$ and $w^{(4)}_{11\infty}/w^{(0)}_1$. The black continuous line signals the onset of solute drag, while the dashed one shows $L_{BV} = -L_{BB}$. The two dotted lines represent the equations $w^{(4)}_{11\infty} = 20w^{(0)}_1$ and $w^{(1)}_{111} = 10w^{(4)}_{11\infty}$.

III. DRAG EFFECT MECHANISM IN THE 16-FREQUENCY MODEL

In a dilute binary alloy, when solute-vacancy interactions are considered up to third-nearest-neighbor sites, 16 different frequencies are required to fully describe the movements of the vacancy among the 42 sites in interaction with the solutes and all their NN sites. Following the notation recalled in Sec. I, $w^{(0)}_1$ describes vacancy jumps in the bulk, far away from any solute atom, and $w^{(2)}_1$ describes the vacancy-solute exchanges. Eight different frequencies describe the jump of the vacancy from a site in interaction with the solute toward another one: $w^{(1)}_{111}$, $w^{(1)}_{121}$, $w^{(1)}_{112}$, $w^{(1)}_{131}$, $w^{(1)}_{113}$, $w^{(1)}_{132}$, $w^{(1)}_{123}$, and $w^{(1)}_{133}$. The next six frequencies describe the dissociation of the vacancy-solute pair ($w^{(3)}_{1\infty1}$, $w^{(3)}_{1\infty2}$, $w^{(3)}_{1\infty3}$) or their association ($w^{(4)}_{11\infty}$, $w^{(4)}_{12\infty}$, $w^{(4)}_{13\infty}$). Figure 5 provides a representation of the displacements to which these frequencies are associated.

The SCMF method used in the 3NN3NN approximation can evaluate the impact on the Onsager matrix of each of the 16 frequencies. The terms of the Onsager matrix are nonlinear functions of the jump frequencies, and so is the case for the drag ratio L_{BV}/L_{BB}. Due to the high number of parameters, a complete parametric study is out of reach. In an ideal model alloy, detailed balance requires each jump frequency w^X_{abc} to be identical to its return jump frequency w^Y_{acb}. The number of parameters required to describe an ideal model alloy from a kinetic point of view is thus reduced to nine different frequencies. To identify the main trends, the independent effect

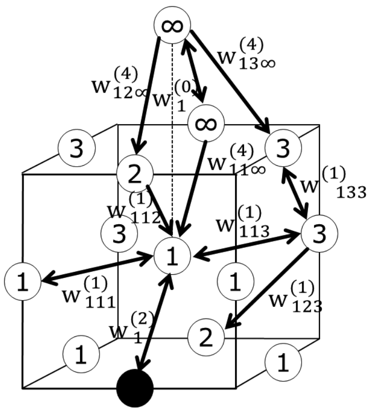

FIG. 5. Vacancy jump frequencies in a dilute fcc binary alloy with third-nearest-neighbor interactions. Arrows indicate the direction of the jumps. The solute atom is represented by a filled circle, and the numbers on lattice sites indicate the distance from the solute atom site while an ∞ indicates sites beyond the range of the interactions. Names of the return jumps have been omitted for the sake of clarity.

of each frequency on such a system is studied. Collective effects involving several frequencies are then investigated. Nonideal alloys have also been studied within two classic models: the linear interpolation of the migration barrier and the broken bond model. These results can be found in the Supplemental Material [44].

A. Independent effect of each frequency

As a first approach, the effect of each frequency is studied by considering an ideal model alloy where all jump frequencies are identical with the exception of a single frequency and the corresponding return jump frequency. Results of SCMF calculations performed in the 3NN3NN approximation for this system are represented in Fig. 6. The drag ratio L_{BV}/L_{BB} is plotted as a function of each frequency while all the others are kept at a fixed identical value. As solute-vacancy exchanges do not change the barycenter of the solute-vacancy pair, the corresponding frequency $w_1^{(2)}$ does not impact the drag ratio. Four different frequencies can lead independently to solute drag: $w_{111}^{(1)}$, $w_{112}^{(1)}$, $w_{113}^{(1)}$, and $w_{13\infty}^{(4)}$. The effect of $w_{111}^{(1)}$, which induces drag by displacements of the vacancy on the "1" orbit, had already been identified in the five-frequency model and remain unchanged. However, the frequency $w_{11\infty}^{(4)}$ of the five-frequency model, that induces drag by displacements of the vacancy on the "1+" orbit, is split in three different ones in the 16-frequency model: increasing $w_{112}^{(1)}$ and $w_{113}^{(1)}$ induces drag, while $w_{11\infty}^{(4)}$ appears to have an opposite effect. This differentiation of the behavior can be understood by observing the fcc structure. As can be seen on Fig. 5, the vacancy can orbit around the solute by alternating either first- and second-nearest-neighbor sites on a so-called "1-2" orbit or first- and third-nearest-neighbor sites on a "1-3" orbit, while the fourth-nearest sites reached from a first-nearest-neighbor site is not neighboring any other first-nearest-neighbor sites, and the vacancy escapes from the solute. This last route thus reduces the drag ratio. These displacements are summarized on Fig. 7, where these pathways are represented in a simplified manner. Finally, jumps between third- and fifth-nearest sites, controlled by the frequency $w_{13\infty}^{(4)}$, also allow the vacancy to orbit around the solute, and thus induces solute drag.

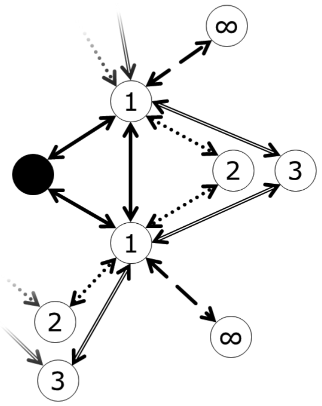

FIG. 7. Schematic pathways of the vacancy around the solute atom in a fcc alloy that involve first-nearest-neighbor sites. The filled circle represents the solute atom, the arrows the possible vacancy-atom exchanges, with a different style of line for each unique site-pairing type.

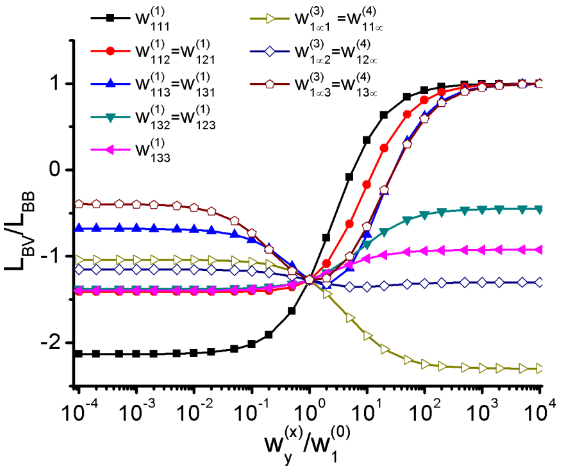

FIG. 6. (Color online) Parametric study of L_{BV}/L_{BB} in a dilute fcc binary alloy within the 16-frequency model. For each curve, all frequencies but the designated one are equal to $w_1^{(0)}$.

B. Collective effect

Figure 6 shows that an increase of the $w_{123}^{(1)}$ or the $w_{133}^{(1)}$ frequency increases the drag ratio. However, this effect is too weak to induce solute drag by the vacancy. As the drag ratio is a nonlinear function of the jump frequencies, collective effects may still appear. The drag ratio has thus been computed in the 3NN3NN approximation as a function of both $w_{123}^{(1)}$ and $w_{133}^{(1)}$ and the results are displayed on Fig. 8. The simultaneous increase of the two frequencies leads to solute drag. This behavior can be explained by observing the fcc structure, which allows the vacancy orbiting around the solute by performing alternatively the two kinds of jumps on a more complex "2-3-3" orbit.

Similarly, the sequence 2-5-3-5 (in NN distance from the solute) can induce solute drag. This path is similar to the "2-4-3-4" orbit of the bcc lattice described in Ref. [25]. In both cases, one of the frequencies involved already allows

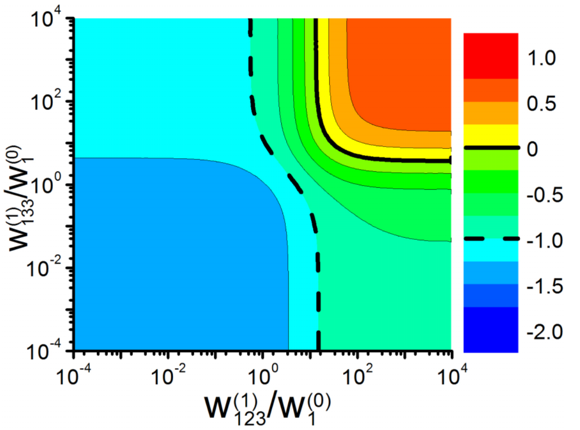

FIG. 8. (Color online) Contour map of L_{BV}/L_{BB} as a function of the $w_{123}^{(1)}$ and $w_{133}^{(1)}$ frequency. The black continuous line signals the onset of solute drag, while the dashed one shows $L_{BV}=-L_{BB}$.

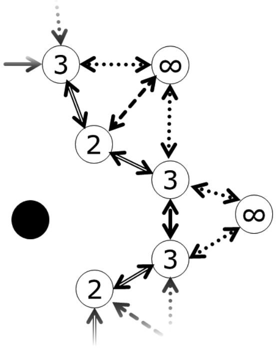

FIG. 9. Schematic pathways of the vacancy around the solute atom in a bcc alloy that do not involve first-nearest-neighbor sites. The filled circle represents the solute atom, the arrows the possible vacancy-atom exchanges, with a different style of line for each type of bond.

solute drag on the simpler "3+" orbit. The pathways involving the third-nearest-neighbor sites are represented on Fig. 9 for the fcc lattice. The $w^{(4)}_{13\infty}$ allows solute drag by motion of the vacancy on the "3+" orbit, which masks the effect of the more complex 2-5-3-5 orbit. As a consequence, this orbit has very little effect on solute drag, as illustrated on Fig. 10. In this figure, the drag ratio is represented as a function of both $w^{(4)}_{12\infty}$ and $w^{(4)}_{13\infty}$ for different values of $w^{(4)}_{11\infty}$. Increasing $w^{(4)}_{12\infty}$ has nearly no effect on the drag ratio when $w^{(4)}_{11\infty} > 1$. However, for $w^{(4)}_{11\infty} \leqslant 1$, an area where solute drag takes place appears at low values of $w^{(4)}_{13\infty}$ and $w^{(4)}_{13\infty}$. This area corresponds to a trapping effect similar to the one observed in the five-frequency model. By reducing simultaneously these three frequencies, an area surrounding the solute atom is isolated from the bulk of the crystal. The trap corresponds this time to the 42 sites that are either first-, second-, or third-nearest neighbor of the solute. A vacancy that enters this zone will then jump many times around the solute before escaping, and will induce solute drag.

IV. PREDICTION OF SOLUTE DRAG IN SPECIFIC ALLOYS

With the improvement of computing capacities, calculations of the exchange frequencies using DFT are becoming more common. Using Vineyard's harmonic transition state equation [47], the frequency $w^{(\zeta)}_{abc}$ can be written as the product of an attempt frequency ν and the exponential of the product of a migration barrier energy E^{mig} and the inverse thermodynamic

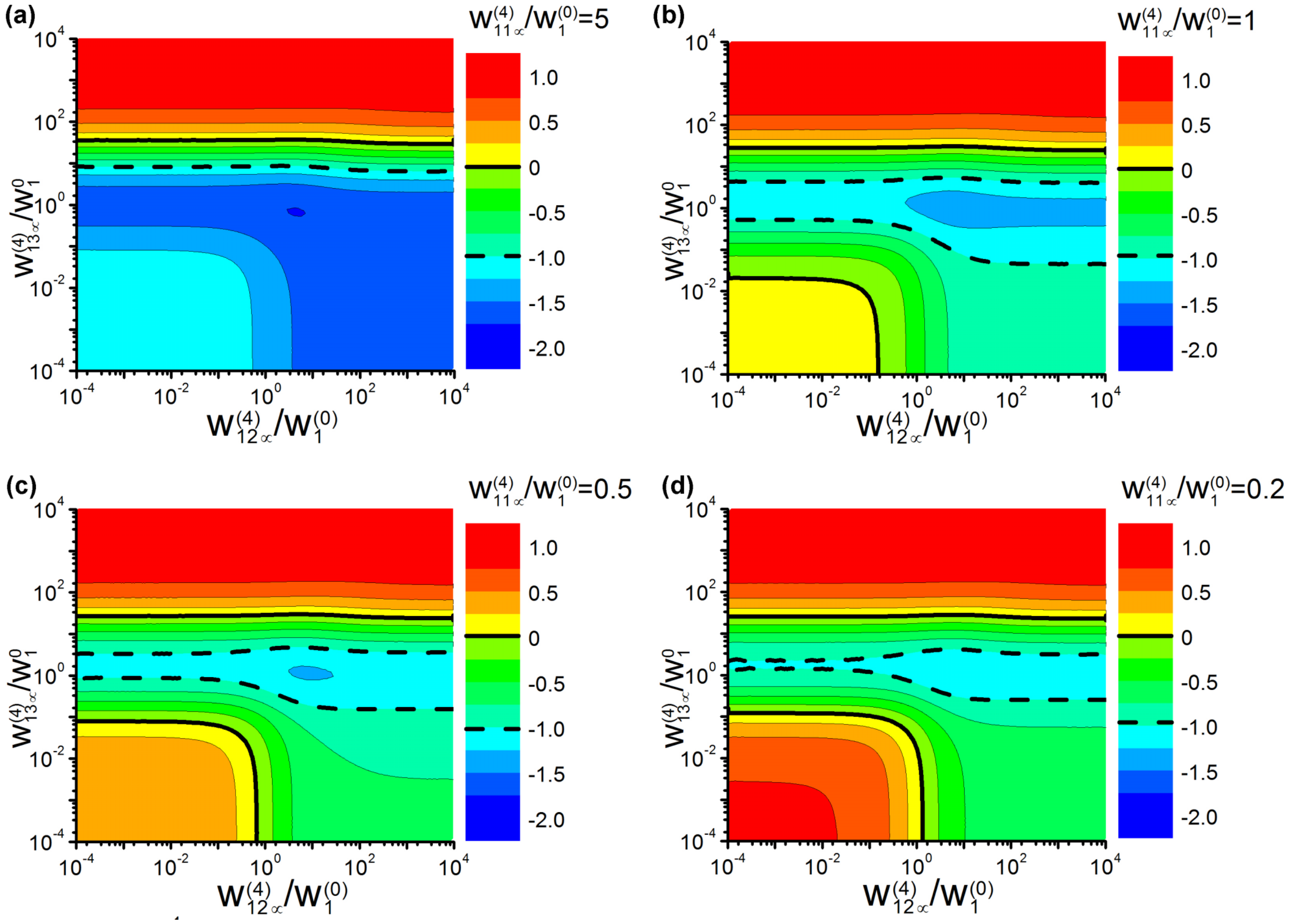

FIG. 10. (Color online) Contour map of the L_{BV}/L_{BB} ratio as a function of the $w^{(4)}_{12\infty}$ and $w^{(4)}_{13\infty}$ frequency. (a) for $w^{(4)}_{11\infty} = 5w_0$, (b) for $w^{(4)}_{11\infty} = w_0$, (c) for $w^{(4)}_{11\infty} = 0.5w_0$, and (d) for $w^{(4)}_{11\infty} = 0.2w_0$. The black continuous line signals the onset of solute drag. The dashed line used for clarity corresponds to $L_{BV} = -L_{BB}$.

temperature $\beta = (k_B T)^{-1}$:

$$w_{abc}^{(\zeta)} = \nu(\zeta,abc)e^{-\beta E^{\mathrm{mig}}(\zeta,abc)}. \tag{3}$$

In the following, the dependencies of ν and E^{mig} on ζ, a, b, and c will be omitted when no confusion is possible. In a bottom-up approach, DFT calculations can provide ν and E^{mig} for each frequency. These results can be used with SCMF calculations to predict the onset of solute drag in specific alloys. Using data from various sources in the literature, drag ratios are computed for various alloys. We evaluate the effect of potential sources of error on the reliability of the results and compare to experimental results.

A. Drag ratio from first-principles calculation

Exchange frequencies for dilute alloys computed from first principles have been published by several groups studying diffusion properties in fcc alloys [33,34,36,48–50]. In the absence of complete analytic model for longer-range interactions, these frequencies have been used within the five-frequency model even when interactions beyond first-NN sites where non-negligible. In that case, as the vacancy can jump from a first-nearest neighbor of the solute towards either a second-, third-, or fifth-nearest-neighbor sites, three different $w_{1\infty 1}^{(3)}$ frequencies and three different $w_{11\infty}^{(4)}$ can be computed. While this fact is ignored in Ref. [33], Refs. [34,36] compute a weighted arithmetic average of the corresponding migration barriers for a 1NN1NN calculation within the five-frequency model.

The resulting five-frequency model can be used to investigate the likelihood of the occurrence of solute drag in specific alloys. The results for the Ni(Cr), Ni(Fe), Ni(Si), Al(Cu), Al(Mg), Al(Si), UC(Zr), and UC(Xe) are presented on Fig. 11. The SCMF calculations were performed in the 1NN, 1NN1NN, and 3NN3NN approximations as a function of temperature. It can be seen that while the 1NN approximation provides sometimes qualitatively wrong results, the 1NN1NN approximation can provide quantitatively acceptable results compared with the 3NN3NN approximation. In these cases, solute drag by vacancies is taking place at low temperature but disappears at higher temperature. However, in many cases solute drag does not take place at low temperatures. In Refs. [49,51], a systematic calculation of the nearest-neighbor binding energy and of the five frequencies for the diffusion of various impurities in Al has been performed. Using 3NN3NN calculations, it was found that in many cases solute drag does not take place at low temperature, when the inequality $w_{111}^{(1)} > w_{11\infty}^{(4)} > w_1^{(0)}$ is verified. To identify the changes of regime for these alloys, the flux ratio $\phi = \frac{1}{c_B}\frac{L_{BV}}{L_{VV}}$ is computed. As in the dilute limit $\phi = -\frac{1}{c_B}\frac{L_{BV}}{L_{AV}}$, a crossover related to the relative diffusion speed of impurities and matrix atoms occurs at $\phi = -1$. For $\phi > 0$, solute drag occurs and an enrichment near vacancy sinks is expected. For $0 > \phi > -1$, the inverse Kirkendall effect results in an enrichment despite the absence of solute drag, while for $\phi < -1$, a depletion of solute atoms near the sink is expected. The temperatures at which $\phi = 0$ and -1 are both presented in Table I as T_{drag} and T_e, together with the orbit responsible for solute drag. Across the different systems, T_{drag} varies from a few tens of Kelvin to more than a thousand. This variation is primarily due to the difference between the migration enthalpies, which range from approximately 0.01 eV for $w_1^{(0)}$ and $w_{11\infty}^{(4)}$ and for Ni(Fe) and for $w_{111}^{(1)}$ and $w_1^{(0)}$ for Al(Mg), and to 0.2 eV for the difference between $w_1^{(0)}$ and $w_{111}^{(1)}$ for Al(Cu). In the case of UC(Xe), the large difference of 0.8 eV between the migration barriers of $w_1^{(0)}$ and $w_{11\infty}^{(4)}$ results in a transition temperature exceeding 2000 K.

In alloy systems where the three association frequencies are significantly different, one expects non-negligible interactions beyond the first-nearest-neighbor distance. Taking these interactions into account is likely to be required to obtain quantitative estimations not only of the Onsager matrix, but also of the diffusion coefficients. The choice of Tucker *et al.* [34] and Bévillon *et al.* [36] to rely on the arithmetic average of the migration barriers corresponding to the different associative or dissociative exchanges to describe the migration barriers of the effective dissociation and association exchanges is a convenient way to obtain a five-frequency model. However, as jump frequencies are exponential functions of the migration barrier, from a mathematical point of view, an average of the jump frequencies and not of the migration barrier would be more suitable, especially at low temperature where the behavior is controlled by the lowest migration barrier. Moreover, the discussion in Sec. III shows that the five-frequency model can be insufficient to describe some solute drag mechanisms. To illustrate the effect of each approximation, we consider a Ni(Si) alloy for which the 16 frequencies required to fully take into account interactions up to the third-NN sites have been computed.

The averaging procedure introduced in Ref. [34] can be performed on this system to reduce it to only 5 frequencies but a full calculation with the 16 frequencies can also be performed.[1] In the Ni(Si) case, the migration barrier of the dissociation jumps $w_{1\infty 1}^{(3)}$, $w_{1\infty 2}^{(3)}$, and $w_{1\infty 3}^{(3)}$ are, respectively, 1.128, 1.066, and 1.068 eV, while the migration barriers of the association jumps $w_{11\infty}^{(4)}$, $w_{12\infty}^{(4)}$, and $w_{13\infty}^{(4)}$ are, respectively, 1.028, 1.077, and 1.112 eV. Figure 12 shows the results obtained by using the 16 frequencies, 5 frequencies averaged using the procedure introduced in Ref. [34] and a truncated set of 5 frequencies where $w_{1\infty 1}^{(3)} = w_{121}^{(3)}$ and $w_{11\infty}^{(4)} = w_{112}^{(4)}$. In the case of the Ni(Si) alloy, the approximation performed by averaging the association frequencies does not impact the qualitative picture concerning solute drag. However, based on the understanding of the origin of solute drag as described in Sec. III, this approximation can provide qualitatively misleading results if $w_{111}^{(1)} < w_1^{(0)}$ and no higher orbit displacement nor trap effect takes place, as it is the case when either $w_{112}^{(1)} < w_1^{(0)} < w_{113}^{(1)}$ or $w_{112}^{(1)} > w_1^{(0)} > w_{113}^{(1)}$ or $w_1^{(0)} < w_{11\infty}^{(4)}$. In these cases, using a more complete model that takes into account interactions up to second- or third-nearest-neighbor distances appears necessary to establish the presence of solute drag.

---

[1] A full calculation that considers third-nearest-neighbor interactions is impossible from the results of Tucker *et al.* or Bevillon *et al.* as only 9 out of the 16 frequencies have been computed.

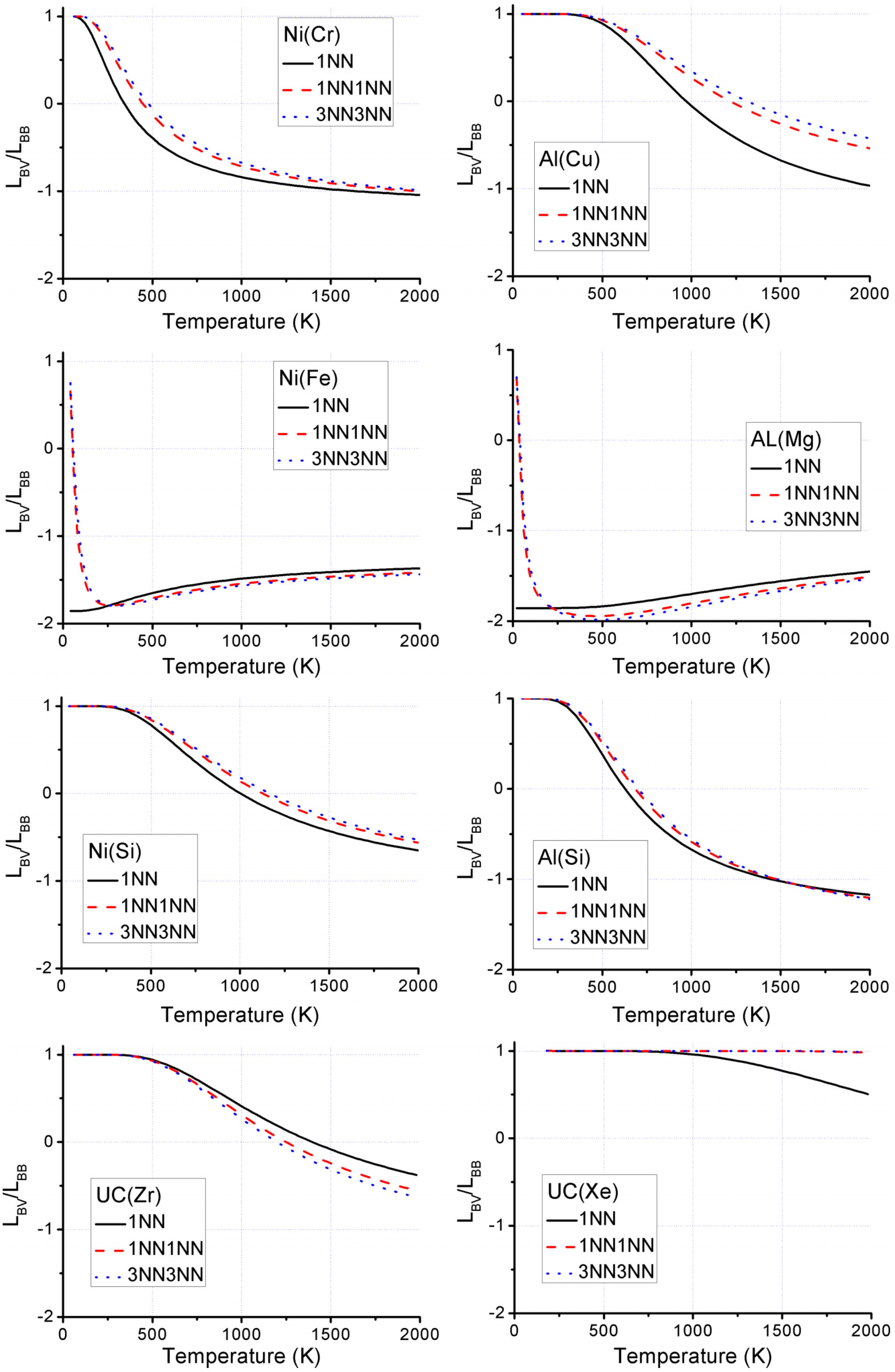

FIG. 11. (Color online) L_{BV}/L_{BB} ratio as a function of the temperature for different alloys described by the five-frequency model. In each case, the L_{BV}/L_{BB} ratio is computed using the 1NN, the 1NN1NN, and the 3NN3NN approximations using data from first-principles calculations from Refs. [33,34,36,48]. When several values for the migration barriers of $w^{(3)}_{1\infty 1}$ and $w^{(4)}_{11\infty}$ are available, the five-frequency model is obtained by averaging the different corresponding migration enthalpies.

B. Reliability of the SCMF prediction of solute drag

The reliability of the solute drag prediction is studied by analyzing potential sources of error. The effect of the truncation of kinetic correlations is first studied. The sensitivity of the results with the input parameters is then explored. Finally, a comparison with experimental results is performed.

TABLE I. Transition temperature between solute drag at low temperature and no drag at high temperature, and between enrichment and depletion regimes for different alloys described by the five-frequency model. When solute drag takes place, the orbit allowing it is provided. Original data are extracted from Refs. [33,34,36,48,49]. *n.t.* stands for no transition.

Matrix	Impurity	T_{drag}	Orbit	T_e (K)	Matrix	Impurity	T_{drag} (K)	Orbit	$T_e(K)$
UC	Xe	>2000 [36]	1	*n.t.*	UC	Zr	1220 [36]	1	*n.t.*
Ni	Cr	400 [34]	1	500	Ni	Fe	40 [34]	1+	40
Ni	Si	1160 [48]	1	1250	Al	Li	240 [49]	1	300
Al	Zr	1800 [49]	1+	*n.t.*	Al	Ho	360 [49]	1+	380
Al	Zn	320 [49]	1	780	Al	Ca	*n.t.* [49]	*n.t.*	*n.t.*
Al	Dy	80 [49]	1+	85	Al	Au	820 [49]	1	*n.t.*
Al	Tl	*n.t.* [49]	*n.t.*	*n.t.*	Al	Sc	840 [49]	1+	*n.t.*
Al	Y	120 [49]	1+	125	Al	Cu	1300 [33], 1100 [49]	1	*n.t.*
Al	In	*n.t.* [49]	*n.t.*	*n.t.*	Al	Lu	640 [49]	1+	900
Al	Tb	40 [49]	1+	40	Al	Ag	380 [49]	1	*n.t.*
Al	Ga	180 [49]	1	890	Al	Tm	500 [49]	1+	560
Al	Mg	40 [33], 80 [49]	1+	40 [33], 85 [49]	Al	Gd	*n.t.* [49]	*n.t.*	170
Al	Pb	*n.t.* [49]	*n.t.*	*n.t.*	Al	Er	320 [49]	1+	330
Al	Sm	*n.t.* [49]	*n.t.*	820	Al	Hg	*n.t.* [49]	*n.t.*	*n.t.*
Al	Sn	*n.t.* [49]	*n.t.*	*n.t.*	Al	Cd	*n.t.* [49]	*n.t.*	1560
Al	Ge	160 [49]	1	2000	Al	Bi	*n.t.* [49]	*n.t.*	*n.t.*
Al	Si	600 [33], 440 [49]	1	*n.t.*	Al	Sb	*n.t.* [49]	*n.t.*	*n.t.*

1. *Convergence with the number of shells*

The SCMF calculation of the Onsager matrix requires truncating the kinetic correlations. The impact of this truncation has been shown in the case of the five-frequency model on Fig. 3. In order to evaluate quantitatively the impact of this truncation on the Onsager matrix, the convergence of the terms of the Onsager matrix has been studied with respect to the number of shells k. The Onsager matrix of a five- (resp. four-) frequency alloy on a fcc (resp. bcc) lattice has been computed in the 1NN(1NN)$^{k-1}$ approximation for various values of k. Assuming the error performed using the 1NN(1NN)$^{7-1}$ approximation to be negligible, we define the relative truncation error $\epsilon_{ij}(k) = \frac{L_{ij}(k)-L_{ij}(7)}{Lij(7)}$ between the values computed using the 1NN(1NN)$^{k-1}$ approximation and the one computed using the 1NN(1NN)$^{7-1}$ approximation. As the bare mobility is not affected by the truncation error, the error is maximum for the nondiagonal terms of the Onsager matrix. As shown on Fig. 13, the terms of the Onsager matrix converge exponentially with the number of shells, following a law $\epsilon_{ij}(k) = AB^{-k}$. The prefactor A varies by several orders of magnitude according to the lattice structure and the values of the ratio $w^{(4)}_{11\infty}/w^{(0)}_1$, while $2.5 < B < 3.5$.

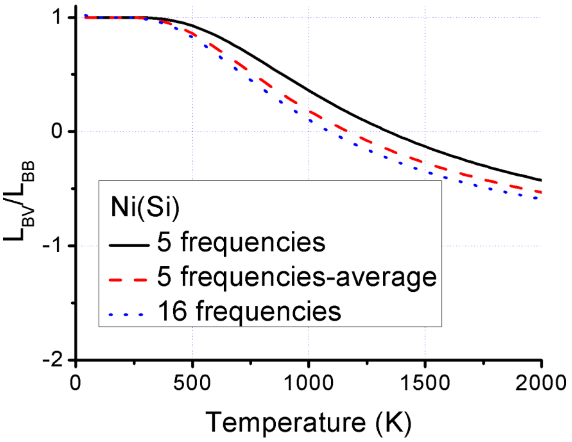

FIG. 12. (Color online) L_{BV}/L_{BB} ratio as a function of the temperature for the Ni(Si) alloy. In each case, the L_{BV}/L_{BB} ratio is computed using the 3NN3NN approximation, using data from first-principles calculations from Ref. [48]. The black continuous line corresponds to a five-frequency model obtained by considering only the $w^{(1)}_{121}$ and $w^{(1)}_{112}$ for the dissociation and association events, the red dashed line corresponds to a five-frequency model obtained by averaging the different jump frequencies corresponding to the dissociation and association events, and the dotted line to the 16-frequency model.

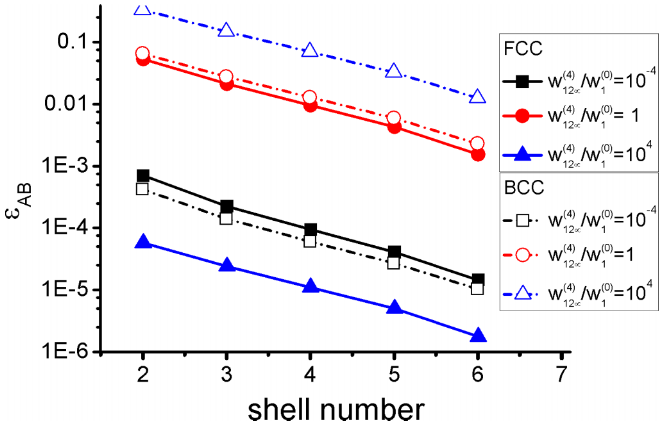

FIG. 13. (Color online) Relative error $\varepsilon_{AB}(k)$ as a function of the number k of shells considered in a SCMF calculation in the 1NN(1NN)$^{k-1}$ approximation for an ideal fcc alloy described by the five-frequency model and on an ideal bcc alloy described by the four-frequency model. Results are displayed for $w^{(2)}_1 = w^{(1)}_{111} = w^{(0)}_1$ and different values of $w^{(4)}_{11\infty}/w^{(0)}_1$.

When $w_{11\infty}^{(4)}/w_{1}^{(0)} = 1$, the L_{BB} term of the Onsager matrix is proportional to the correlation factor f. Let $\langle\cos(\theta)\rangle$ be the average angle between two consecutive jumps of the vacancy; the correlation factor can be written as $f = 1 + 2\sum_q \langle\cos(\theta)\rangle^q$, where each term corresponds to the correlation induced by a sequence of q consecutive jumps [52]. By truncating the correlation beyond the kth shell, a SCMF calculation performs an exact calculation of the correlations due to a sequence of k jumps, but induces a partial truncation of the terms for $q > k$, which results in an exponentially decreasing error. If high accuracy is required for a calculation of the Onsager matrix, this exponential convergence could be used to extrapolate the results obtained for a low value of the number of shells.

2. *Sensitivity to the prefactors*

Solute drag depends on the relative values of the different frequencies. DFT calculations are now able to provide accurate data for the migration barriers, but determination of the prefactor is a more difficult task [33,48]. Even if the frequencies are mostly determined by the migration barriers, the question of the effect of inaccuracies on the prefactor remains. To study this problem, we used two examples from the alloys presented in the previous section. We studied the effect of a variation of the prefactors ν_1 and ν_4 of the frequencies $w_{111}^{(1)}$ and $w_{11\infty}^{(4)}$ on the crossover temperature of the onset of solute drag. For that purpose, values ν that differ from the original prefactors ν^* by a factor within $[\frac{1}{2},2]$ were used to estimate the impact of an error on the prefactors. As our point is not to study the effect of a variation of the binding free energy, the frequencies $w_{1\infty 1}^{(3)}$ and $w_{11\infty}^{(3)}$ have been modified similarly. The results are being displayed on Fig. 14.

In the case of the Ni(Fe) alloy, solute drag is due to the "1+" orbit, controlled by the $w_{11\infty}^{(4)}$ frequency. The crossover temperature is then completely insensitive to the value of ν_1, but varies substantially with ν_4. In the case of the Al(Cu) alloy, solute drag is instead due to the "1" orbit, controlled by the $w_{111}^{(1)}$ frequency. The crossover temperature is then very sensitive to the values of ν_1, but a lesser and nonlinear dependency with ν_4 also appears. Thus, it appears that the value of the prefactor of the frequency controlling the orbit causing solute drag has a non-negligible effect on the crossover temperature, while the impact of the other is much lesser. As a consequence, in order to accurately predict solute drag in a given alloy, the prefactors of the frequencies controlling that orbit need to be carefully evaluated. This sensitivity to the attempt frequencies can also be translated in terms of accuracy of the migration barrier. As an error of the order of 10 meV on the migration barrier corresponds to multiplying the jump frequency by a factor 1.5 at room temperature, an accuracy of the migration barrier of the order of a few meV is required.

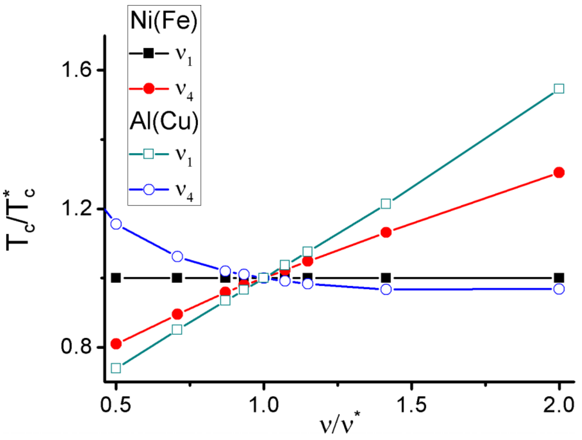

FIG. 14. (Color online) Temperature T_{drag} of onset of solute drag as a function of the prefactor for the Ni(Fe) and Al(Cu) alloys. Prefactors ν_1 and ν_4 are varied independently. Both the temperature and the prefactors are normalized by the values of the original model T_c^* and ν^*.

3. *Comparison with experiments*

Using results from different experiments [18,53–56], flux ratios have been computed for several alloys on fcc lattices [19]. Results presented in Refs. [54,56] can be compared to some extent with the DFT data for the Al(Ge), Al(Mg), Al(Zn), and Al(Cu) alloys presented in Sec. IV A. These experiments, conducted near the melting temperature T_{melt} of aluminum at, respectively, $T = 860\text{ K} = 0.92T_{\text{melt}}$ and $T = 760\text{ K} = 0.81T_{\text{melt}}$, provide estimates of the ratios of solute flux over the vacancy $\frac{J_B}{c_B(J_V)}$, which is equal in these experiments to the ratio $\frac{1}{c_B}\frac{L_{BV}}{L_{VV}}$. In the cases of Al(Ge), a depletion of solute near the sink is found, which corresponds to a flux ratio below -1. In the case of Al(Zn) and Al(Mg), an enrichment near the sink is found, which indicates a flux ratio larger than -1. Finally, in the case of Al(Cu), no segregation could be measured and this inconclusive result is interpreted as the indication of a flux ratio equal to -1.

These results, presented in Table II, can be compared to the results of DFT calculations. The sign of the flux ratio is correctly predicted by DFT calculations in the case of Zn, Ge, and Mg impurities. However, a qualitative disagreement appears in all cases, with DFT calculations predicting an enrichment of Ge and Cu and a depletion of Mg and Zn. Similarly, the results of interdiffusion experiments can be interpreted using the Onsager matrix. Reference [57] provides experimental determinations of the ratio of diffusivity in the Al(Zn) alloy. In the dilute limit, they can be expressed as functions of the terms of the Onsager matrix

$$\frac{D_B}{D_A} = \frac{\frac{L_{BB}}{C_B} - \frac{L_{AB}}{C_A}}{\frac{L_{AA}}{C_A} - \frac{L_{AB}}{C_B}}. \tag{4}$$

TABLE II. Flux ratios $\frac{1}{c_B}\frac{J_B}{(J_V)}$ at 760 K for the Al(Mg) system and 860 K for the other alloys according to the DFT data from Ref. [49] and experimental data from Ref. [19] and references therein.

System	DFT flux ratio	Experimental flux ratio
Al(Ge)	-0.39	-1.92
Al(Mg)	-3.54	>-1
Al(Zn)	-1.15	-0.92
Al(Cu)	0.64	-1

These experiments, performed at 830 K for Al(Zn), provide for this ratio a value of 1.7, while a calculation based on the five frequencies obtained by Simonovic and Sluiter [49] provides a value of 1.1.

The discrepancies between DFT and experimental results might have several origins. First, the accuracy of DFT results can be questioned. The sensitivity of the crossover temperature on the prefactors has been studied in Sec. IV B 2 and can be partly responsible for the discrepancy as it was shown it could modify the transition temperature by a factor 2. Moreover, these models are based on a calculation including a single dissociation frequency. As discussed in Sec. IV A, this reduction to the five-frequency model might also cause the disagreement observed. The presence of solute-vacancy interactions beyond the first-NN sites would change the diffusion properties. However, several experimental causes can explain the disagreement. The experiments have been performed at high temperature, in the vicinity of the melting point. At these temperatures, the energy landscape is modified due to thermal expansion or lattice vibration. None of these high-temperature effects have been considered in the DFT data available for this problem. Also, high temperatures increase the concentration of divacancies and introduce a competing diffusion mechanism; sinks generate strain fields that can alter the diffusion properties [48]. Finally, the interpretation of these experiments includes some approximations. Specifically, they rely on the hypothesis of a negligible gradient of solute concentration, which is valid only in the initial state. Thus, the final result could be affected by the formation of gradients of solute concentration.

V. CONCLUSION

The goal of this study was to explore the onset of solute drag in fcc alloys, to identify the mechanisms involved, and to evaluate the reliability of theoretical prediction of solute drag. To that end, we analytically calculated the Onsager matrix in dilute fcc alloys with solute-vacancy interactions up to third-nearest-neighbor sites and with extended kinetic correlations. One of the first results of this paper is the derivation of analytic expressions for the Onsager coefficients in this case. Comparison with AKMC simulations and a study of the convergence of SCMF calculation with respect to the number of shells considered for the calculation of the kinetic correlation showed that SCMF results converge exponentially and that the 3NN3NN approximation is often a reliable method to predict solute drag. The onset of solute drag has been studied using this approximation. We identified several paths for the vacancy to orbit around the solute atoms. Collective effects, involving different types of jumps with low escape frequencies, can also trigger solute drag if they isolate an orbit around the solute from the matrix. Calculations applied to a model dilute alloy with interactions up to third-nearest-neighbor sites identified cases where solute drag could take place. Using DFT data from previous works, we found solute drag by vacancies under a broad set of conditions; solute drag should be considered as a fairly common phenomenon at low temperatures. Unfortunately, no experimental data of solute drag is available at low temperature to confirm the results obtained numerically, and many reasons can explain the discrepancies found at high temperature. Finally, in order to guide future DFT studies of diffusion, a study of the sensitivity of solute drag to the attempt frequencies has been performed. We demonstrate that the crossover temperature can be very sensitive to the prefactors of some jump frequencies. This study shows that qualitative effects of the relative values of the attempt frequencies can not be dismissed. Despite this sensitivity, the combined use of DFT results with SCMF calculations provides a powerful tool for the prediction of solute drag in alloys, including the onset temperature.

ACKNOWLEDGMENTS

The authors thank M. Mantina for providing extra information on her calculations. This research is partly supported by the DOE-BES Grant No. DE-FG02-05ER46217, and by the DOE-BES Computation Materials and Chemical Sciences Network on "Computational Microstructure Science."

APPENDIX: ANALYTIC EXPRESSIONS FOR 3NN3NN SCMF COMPUTATIONS IN fcc ALLOYS

We consider an alloy on a Bravais lattice under a homogeneous gradient of chemical potential oriented by the unit vector $\vec{u}$. A state of the alloy is defined by a vector $\mathbf{n}$, the component of which are the occupation numbers of all species on all sites $\{n_1^A, n_1^B, \ldots, n_1^v, n_2^A, \ldots\}$ such that $n_i^X = 1$ if the site i is occupied by the species $X \in \{v, A, B, \ldots\}$ and zero otherwise. Let $\alpha,\beta,\gamma,\eta,\zeta$ designate atomic species, $\vec{e}_{is}$ be the vectors linking sites i and s in a system of volume V^{tot}, $\vec{v}$ be a unit vector in the direction of diffusion, and $\vec{u}$ be the unit vector in the direction of the gradient of chemical potential. As detailed in Ref. [25], the Onsager matrix can be written as

$$L_{\vec{v},\vec{u}}^{\alpha\beta} = \frac{1}{2V^{\mathrm{tot}}} \sum_{is} \left[\left(l_{\overline{is},(0)}^{\alpha\beta} \vec{e}_{is} - 2 \sum_{\overline{mj},\overline{pq},\gamma,\sigma,\zeta} \Lambda_{\overline{is},\overline{mj}}^{\alpha,\alpha\gamma} (T^{-1})_{\overline{mj},\overline{pq}}^{\alpha\gamma,\sigma\zeta} \vec{M}_{\overline{pq}}^{\sigma\zeta,\beta} \right) \cdot \vec{u} \right] \vec{e}_{is} \cdot \vec{v}, \tag{A1}$$

where the first sum is performed over all the pairs of sites i,s. The values of the different elements involved in this equation are provided here in the case of the 3NN3NN approximations for a fcc dilute binary alloy. They are also made available in the Supplemental Material [44] together with a Matlab® routine that computes directly the Onsager matrix from a set of 16 frequencies. In a structure with a cubic symmetry like the fcc structure, the diffusion properties are isotropic and we can write $L^{\alpha\beta}_{\vec{v},\vec{u}} = L_{\alpha\beta}$.

For the sake of simplicity, we introduce a compact notation of the three-point averages $W^{(\zeta)}_{abc} = \langle n^\alpha_i n^\beta_j n^v_s w^\zeta_{abc}\rangle$, where a is the distance between sites i and s, b is the distance between the sites i and j, and c the distance between j and s and the indices ζ,a,b,c refer to the four-index systematic nomenclature defined in Sec. I. Using the notations c_B for the concentration in solute B, c_v for the concentration of vacancies and $y^{Bv}_d = e^{-\beta F(d)}$ for the exponential of the binding energy between a vacancy and a solute at a distance d, these quantities take the values

$$\begin{aligned} W^\zeta_{abc} &= c_v c_B y^{Bv}_a w^\zeta_{abc} \quad \text{if} \quad \zeta = 2 \\ &= c_v c_B y^{Bv}_c w^\zeta_{abc} \quad \text{otherwise.} \end{aligned} \tag{A2}$$

Similarly, we group in a single short notation the two-point averages $\mathfrak{X}^{(\zeta)}_{abc} = \langle n^\alpha_i n^v_s w^\zeta_{abc}\rangle$:

$$\begin{aligned} &\mathfrak{X}^\zeta_{abc} = c_v\big[1 - c_B\big(17 + 12y^{Bv}_1 + 6y^{Bv}_2 + 24y^{Bv}_3\big)\big]w^\zeta_{abc} \quad \text{if} \\ &\quad \zeta = 0 = W^\zeta_{abc} \quad \text{otherwise.} \end{aligned} \tag{A3}$$

We use the notation A for the matrix species, B for the solute species, and $T = R + \text{Diag}(D)$. For a binary alloy, only the effective interactions associated to the pair of species $A - B$ needs to be considered. As a consequence, T is an $n \times n$ matrix where n is the number of symmetry classes considered. A vector belonging to each of the symmetry classes can be used to represent them. These vectors are provided in Table III, and Fig. 15 shows these vectors on a fcc lattice. The indices of the symmetry classes in Table III and Fig. 15 correspond also to the order in which they are being used in the following symbolic expressions.

TABLE III. Cartesian coordinates $[x,y,z]$ in lattice constants of a representative of each of the bond classes, for diffusion in the [100] direction. The indices in this table are identical to the row or column numbers used in the symbolic quantities expressions (cf. Fig. 15).

Index	Vector	Index	Vector
1	$\frac{a}{2}[110]$	12	$a[200]$
2	$a[100]$	13	$\frac{a}{2}[411]$
3	$\frac{a}{2}[121]$	14	$\frac{a}{2}[331]$
4	$\frac{a}{2}[211]$	15	$\frac{a}{2}[141]$
5	$a[110]$	16	$a[120]$
6	$\frac{a}{2}[131]$	17	$a[210]$
7	$\frac{a}{2}[311]$	18	$\frac{a}{2}[133]$
8	$a[111]$	19	$\frac{a}{2}[323]$
9	$\frac{a}{2}[132]$	20	$a[112]$
10	$\frac{a}{2}[231]$	21	$a[211]$
11	$\frac{a}{2}[321]$		

$$R = \left(\begin{array}{ccccccccccccccccccccc}
0 & -W^{(1)}_{121} & -2W^{(1)}_{131} & -2W^{(1)}_{131} & -W^{(3)}_{1\infty1} & 0 & 0 & 0 & 0 & 0 & 0 & 0 & 0 & 0 & 0 & 0 & 0 & 0 & 0 & 0 & 0 \\
-4W^{(1)}_{112} & 0 & 0 & -4W^{(1)}_{132} & 0 & 0 & -4W^{(3)}_{1\infty2} & 0 & 0 & 0 & 0 & 0 & 0 & 0 & 0 & 0 & 0 & 0 & 0 & 0 & 0 \\
-W^{(1)}_{113} & 0 & 0 & -W^{(1)}_{133} & -W^{(3)}_{1\infty3} & -W^{(3)}_{1\infty3} & 0 & -W^{(3)}_{1\infty3} & -W^{(3)}_{1\infty3} & -W^{(3)}_{1\infty3} & 0 & 0 & 0 & 0 & 0 & 0 & 0 & 0 & 0 & 0 & 0 \\
-2W^{(1)}_{113} & -W^{(1)}_{123} & -2W^{(1)}_{133} & 0 & -2W^{(3)}_{1\infty3} & 0 & -2W^{(3)}_{1\infty3} & -W^{(3)}_{1\infty3} & 0 & 0 & -2W^{(3)}_{1\infty3} & 0 & 0 & 0 & 0 & 0 & 0 & 0 & 0 & 0 & 0 \\
-W^{(4)}_{11\infty} & 0 & -2W^{(4)}_{13\infty} & -2W^{(4)}_{13\infty} & 0 & -W^{(0)}_1 & -W^{(0)}_1 & 0 & 0 & -2W^{(0)}_1 & -2W^{(0)}_1 & 0 & 0 & -W^{(0)}_1 & 0 & 0 & 0 & 0 & 0 & 0 & 0 \\
0 & 0 & -2W^{(4)}_{13\infty} & 0 & -W^{(0)}_1 & 0 & 0 & 0 & 0 & -2W^{(0)}_1 & 0 & 0 & -2W^{(0)}_1 & 0 & 0 & 0 & -W^{(0)}_1 & 0 & 0 & 0 & 0 \\
0 & -W^{(4)}_{12\infty} & 0 & -2W^{(4)}_{13\infty} & -W^{(0)}_1 & 0 & 0 & 0 & 0 & 0 & -2W^{(0)}_1 & -W^{(0)}_1 & 0 & 0 & 0 & -2W^{(0)}_1 & 0 & -W^{(0)}_1 & 0 & 0 & 0 \\
0 & 0 & -2W^{(4)}_{13\infty} & -W^{(4)}_{13\infty} & 0 & 0 & 0 & 0 & -2W^{(0)}_1 & -2W^{(0)}_1 & -2W^{(0)}_1 & 0 & 0 & 0 & 0 & 0 & 0 & -W^{(0)}_1 & -2W^{(0)}_1 & 0 & 0 \\
0 & 0 & -W^{(4)}_{13\infty} & 0 & 0 & 0 & 0 & -W^{(0)}_1 & 0 & -W^{(0)}_1 & 0 & 0 & -W^{(0)}_1 & 0 & 0 & 0 & 0 & -W^{(0)}_1 & 0 & -W^{(0)}_1 & 0 \\
0 & 0 & -W^{(4)}_{13\infty} & 0 & -W^{(0)}_1 & -W^{(0)}_1 & 0 & -W^{(0)}_1 & -W^{(0)}_1 & 0 & -W^{(0)}_1 & 0 & -W^{(0)}_1 & -W^{(0)}_1 & 0 & -W^{(0)}_1 & 0 & 0 & -W^{(0)}_1 & -W^{(0)}_1 & 0 \\
0 & 0 & 0 & -W^{(4)}_{13\infty} & -W^{(0)}_1 & 0 & -W^{(0)}_1 & -W^{(0)}_1 & 0 & -W^{(0)}_1 & 0 & 0 & 0 & -W^{(0)}_1 & -W^{(0)}_1 & 0 & -W^{(0)}_1 & 0 & -W^{(0)}_1 & 0 & -W^{(0)}_1 \\
0 & 0 & 0 & 0 & 0 & 0 & -4W^{(0)}_1 & 0 & 0 & 0 & 0 & 0 & 0 & 0 & -4W^{(0)}_1 & 0 & 0 & 0 & 0 & 0 & 0 \\
0 & 0 & 0 & 0 & 0 & -W^{(0)}_1 & 0 & 0 & -W^{(0)}_1 & -W^{(0)}_1 & 0 & 0 & 0 & 0 & 0 & -W^{(0)}_1 & 0 & 0 & 0 & -W^{(0)}_1 & 0 \\
0 & 0 & 0 & 0 & -W^{(0)}_1 & 0 & 0 & 0 & 0 & -2W^{(0)}_1 & -2W^{(0)}_1 & 0 & 0 & 0 & 0 & -W^{(0)}_1 & -W^{(0)}_1 & 0 & 0 & 0 & 0 \\
0 & 0 & 0 & 0 & 0 & 0 & -2W^{(0)}_1 & 0 & 0 & 0 & -2W^{(0)}_1 & -W^{(0)}_1 & 0 & 0 & 0 & 0 & -2W^{(0)}_1 & 0 & 0 & 0 & -W^{(0)}_1 \\
0 & 0 & 0 & 0 & 0 & -W^{(0)}_1 & 0 & 0 & 0 & -2W^{(0)}_1 & 0 & 0 & -2W^{(0)}_1 & -W^{(0)}_1 & 0 & 0 & 0 & 0 & 0 & 0 & 0 \\
0 & 0 & 0 & 0 & 0 & 0 & -W^{(0)}_1 & 0 & 0 & 0 & -2W^{(0)}_1 & 0 & 0 & -W^{(0)}_1 & -2W^{(0)}_1 & 0 & 0 & 0 & 0 & 0 & 0 \\
0 & 0 & 0 & 0 & 0 & 0 & 0 & -W^{(0)}_1 & -2W^{(0)}_1 & 0 & 0 & 0 & 0 & 0 & 0 & 0 & 0 & 0 & -2W^{(0)}_1 & -2W^{(0)}_1 & 0 \\
0 & 0 & 0 & 0 & 0 & 0 & 0 & -W^{(0)}_1 & 0 & -W^{(0)}_1 & -W^{(0)}_1 & 0 & 0 & 0 & 0 & 0 & 0 & -W^{(0)}_1 & 0 & -W^{(0)}_1 & -W^{(0)}_1 \\
0 & 0 & 0 & 0 & 0 & 0 & 0 & 0 & -W^{(0)}_1 & -W^{(0)}_1 & 0 & 0 & -W^{(0)}_1 & 0 & 0 & 0 & 0 & -W^{(0)}_1 & -W^{(0)}_1 & 0 & 0 \\
0 & 0 & 0 & 0 & 0 & 0 & 0 & 0 & 0 & 0 & -2W^{(0)}_1 & 0 & 0 & 0 & -W^{(0)}_1 & 0 & 0 & 0 & -2W^{(0)}_1 & 0 & 0
\end{array}\right), \tag{A4}$$

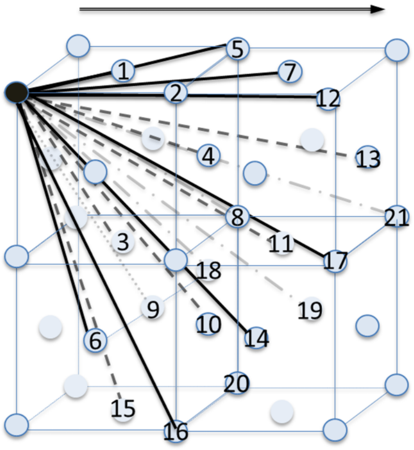

FIG. 15. (Color online) Schematic representation of the classes of bonds associated to the different rows and column of the T matrix. The number on an atomic site is the class represented by the vector linking the filled site to this site. The arrow represents the direction of diffusion.

$$D = \begin{pmatrix} 2W_{111}^{(1)} + 2W_{121}^{(1)} + 4W_{131}^{(1)} + 2W_{1}^{(2)} + W_{1\infty 1}^{(3)} \\ 4W_{112}^{(1)} + 4W_{132}^{(1)} + 4W_{1\infty 2}^{(3)} \\ 2W_{113}^{(1)} + W_{123}^{(1)} + W_{133}^{(1)} + 7W_{1\infty 3}^{(3)} \\ 2W_{113}^{(1)} + W_{123}^{(1)} + 2W_{133}^{(1)} + 7W_{1\infty 3}^{(3)} \\ 7W_{1}^{(0)} + W_{11\infty}^{(4)} + 4W_{13\infty}^{(4)} \\ 9W_{1}^{(0)} + W_{12\infty}^{(4)} + 2W_{13\infty}^{(4)} \\ 7W_{1}^{(0)} + W_{12\infty}^{(4)} + 2W_{13\infty}^{(4)} \\ 9W_{1}^{(0)} + 3W_{13\infty}^{(4)} \\ 10W_{1}^{(0)} + W_{13\infty}^{(4)} \\ 11W_{1}^{(0)} + W_{13\infty}^{(4)} \\ 10W_{1}^{(0)} + W_{13\infty}^{(4)} \\ 12W_{1}^{(0)} \\ 12W_{1}^{(0)} \\ 12W_{1}^{(0)} \\ 12W_{1}^{(0)} \\ 12W_{1}^{(0)} \\ 12W_{1}^{(0)} \\ 12W_{1}^{(0)} \\ 11W_{1}^{(0)} \\ 12W_{1}^{(0)} \\ 12W_{1}^{(0)} \end{pmatrix}, \quad \text{(A5)}$$

$$(\vec{M}^{AB,A}) \cdot \vec{u} = \frac{a}{2} \begin{pmatrix} 2W_{111}^{(1)} - 2W_{131}^{(1)} - W_{1\infty 1}^{(3)} \\ 4W_{112}^{(1)} - 4W_{1\infty 2}^{(3)} \\ W_{113}^{(1)} + W_{123}^{(1)} - W_{133}^{(1)} - W_{1\infty 3}^{(3)} \\ 2W_{113}^{(1)} + 2W_{133}^{(1)} - 4W_{1\infty 3}^{(3)} \\ W_{11\infty}^{(4)} - 3W_{1}^{(0)} + 2W_{13\infty}^{(4)} \\ W_{12\infty}^{(4)} - W_{1}^{(0)} \\ W_{12\infty}^{(4)} - 3W_{1}^{(0)} + 2W_{13\infty}^{(4)} \\ 2W_{13\infty}^{(4)} - 2W_{1}^{(0)} \\ 0 \\ W_{13\infty}^{(4)} - W_{1}^{(0)} \\ W_{13\infty}^{(4)} - W_{1}^{(0)} \\ 0 \\ 0 \\ 0 \\ 0 \\ 0 \\ 0 \\ 0 \\ 0 \\ 0 \\ 0 \end{pmatrix}, \quad \text{(A6)}$$

$$(\vec{M}^{AB,B}) \cdot \vec{u} = \frac{a}{2} c_b c_v \begin{pmatrix} -W_{1}^{(2)} \\ 0 \\ 0 \\ 0 \\ 0 \\ 0 \\ 0 \\ 0 \\ 0 \\ 0 \\ 0 \\ 0 \\ 0 \\ 0 \end{pmatrix}, \quad \text{(A7)}$$

$$(\Lambda^{A,AB}) = c_b c_v \begin{pmatrix} 2W^{(1)}_{111} - 2W^{(1)}_{131} - W^{(3)}_{1\infty 1} \\ W^{(1)}_{112} - W^{(3)}_{1\infty 2} \\ 2W^{(1)}_{113} + 2W^{(1)}_{123} - 2W^{(1)}_{133} - 2W^{(3)}_{1\infty 3} \\ 2W^{(1)}_{113} + 2W^{(1)}_{133} - 4W^{(3)}_{1\infty 3} \\ W^{(4)}_{11\infty} - 3W^{(0)}_{1} + 2W^{(4)}_{13\infty} \\ W^{(4)}_{12\infty} - W^{(0)}_{1} \\ W^{(4)}_{12\infty} - 3W^{(0)}_{1} + 2W^{(4)}_{13\infty} \\ 2W^{(4)}_{13\infty} - 2W^{(0)}_{1} \\ 0 \\ 2W^{(4)}_{13\infty} - 2W^{(0)}_{1} \\ 2W^{(4)}_{13\infty} - 2W^{(0)}_{1} \\ 0 \\ 0 \\ 0 \\ 0 \\ 0 \\ 0 \\ 0 \\ 0 \\ 0 \\ 0 \end{pmatrix}, \tag{A8}$$

$$(\Lambda^{B,BA}) = \begin{pmatrix} W^{(2)}_{1} \\ 0 \\ 0 \\ 0 \\ 0 \\ 0 \\ 0 \\ 0 \\ 0 \\ 0 \\ 0 \\ 0 \\ 0 \\ 0 \end{pmatrix}. \tag{A9}$$

As jumps are limited to nearest-neighbor sites only, there is a single class of nonzero contribution to the bare mobility

$$\begin{aligned} l^{AA}_{(0)} &= \mathfrak{X}^{(0)}_{1} + 2\mathfrak{X}^{(1)}_{112} + 2\mathfrak{X}^{(1)}_{121} + 4\mathfrak{X}^{(1)}_{113} + 4\mathfrak{X}^{(1)}_{131} + 4\mathfrak{X}^{(1)}_{111} + 2\mathfrak{X}^{(1)}_{123} + 2\mathfrak{X}^{(1)}_{132} + 4\mathfrak{X}^{(1)}_{133} + \mathfrak{X}^{(3)}_{1\infty 1} + 2\mathfrak{X}^{(3)}_{1\infty 2} + 14\mathfrak{X}^{(3)}_{1\infty 3} \\ &\quad + \mathfrak{X}^{(4)}_{11\infty} + 2\mathfrak{X}^{(4)}_{12\infty} + 14\mathfrak{X}^{(4)}_{13\infty}, \\ l^{BB}_{(0)} &= \mathfrak{X}^{(2)}_{1}. \end{aligned} \tag{A10}$$

As an example, the substitution of the different short notations is performed for the bare mobility:

$$\begin{aligned} l^{AA}_{(0)} &= c_v w^{(0)}_{1}(1 - c_b y_1) + c_b c_v\big[\big(w^{(4)}_{11\infty} - w^{(0)}_{1}\big) + 2\big(w^{(4)}_{12\infty} - w^{(0)}_{1}\big) + 14\big(w^{(4)}_{13\infty} - w^{(0)}_{1}\big) + 4y_1\big(w^{(1)}_{111} - w^{(0)}_{1}\big) + 2y_2\big(w^{(1)}_{112} - w^{(0)}_{1}\big) \\ &\quad + 4y_3\big(w^{(1)}_{113} - w^{(0)}_{1}\big) + 2y_1\big(w^{(1)}_{121} - w^{(0)}_{1}\big) + 2y_3\big(w^{(1)}_{123} - w^{(0)}_{1}\big) + 4y_1\big(w^{(1)}_{131} - w^{(0)}_{1}\big) + 2y_2\big(w^{(1)}_{132} - w^{(0)}_{1}\big) + 4y_3\big(w^{(1)}_{133} - w^{(0)}_{1}\big) \\ &\quad + y_1\big(w^{(3)}_{1\infty 1} - w^{(0)}_{1}\big) + 2y_2\big(w^{(3)}_{1\infty 2} - w^{(0)}_{1}\big) + 14y_3\big(w^{(3)}_{1\infty 3} - w^{(0)}_{1}\big)\big], \\ l^{BB}_{(0)} &= c_b c_v w^{(2)}_{1} y_1. \end{aligned} \tag{A11}$$

[1] V. I. Yelagin, V. V. Zakharov, S. G. Pavlenko, and T. D. Rostova, Phys. Met. Metall. **60**, 88 (1985).

[2] E. Clouet, L. Laé, T. Épicier, W. Lefebvre, M. Nastar, and A. Deschamps, Nat. Mater. **5**, 482 (2006).

[3] F. Danoix, E. Bemont, P. Maugis, and D. Blavette, Adv Eng. Mater. **8**, 1202 (2006).

[4] Z. Mao, C. K. Sudbrack, K. E. Yoon, G. Martin, and D. N. Seidman, Nat. Mater. **6**, 210 (2007).

[5] G. Martin, R. Cauvin, and A. Barbu, *Phase Transformations During Irradiation* (Applied Science, London, 1983), p. 47.

[6] S. Shu, P. Bellon, and R. S. Averback, Phys. Rev. B **87**, 144102 (2013).

[7] A. Barbu and G. Martin, Scr. Metall. **11**, 771 (1977).

[8] A. Barbu, G. Martin, and A. Chamberod, J. Appl. Phys. **51**, 6192 (1980).

[9] M. Nastar and F. Soisson, *Comprehensive Nuclear Materials* (Elsevier, Amsterdam, 2012), p. 471.

[10] Z. Jiao and G. Was, Acta Mater. **59**, 1220 (2011).

[11] M. Nastar, Philos. Mag. A **85**, 641 (2005).

[12] A. J. Ardell, *Materials Issues for Generation IV Systems*, NATO Science for Peace and Security Series B: Physics and Biophysics (Springer, Berlin, 2008), pp. 285–310.

[13] A. Barbu and A. J. Ardell, Scr. Metall. **9**, 1233 (1975).

[14] H. Wan, Y. Shen, X. Jin, Y. Chen, and J. Sun, Acta Mater. **60**, 2528 (2012).

[15] P. Bellon, *Comprehensive Nuclear Materials* (Elsevier, Amsterdam, 2012), Chap. 1.15, pp. 411–432.

[16] T. Garnier and M. Nastar, Phys. Rev. B **88**, 134207 (2013).

[17] J. Ågren, Met. Mater. Trans. A **43**, 3453 (2012).

[18] T. Anthony, J. Appl. Phys. **41**, 3969 (1970).

[19] T. Anthony, *Proceedings of the Conference on Atomic Transport in Solids and Liquids, Marstransd*, 1970 (Verlag der Zeitschrift für Naturforschung, Tübingen, 1971), p. 138.

[20] T. Anthony, *Proceedings of the Conference on Radiation-Induced Voids in Metals, Albany* (US Atomic Energy Commission, State University of New York, Albany, 1972), p. 630.

[21] A. Smigelskas and E. Kirkendall, Trans. AIME **171**, 130 (1947).

[22] A. Gusak and K. Tu, Acta Mater. **57**, 3367 (2009).

[23] T. Anthony, Acta Metall. **17**, 603 (1969).

[24] A. R. Allnatt and A. B. Lidiard, *Atomic Transport in Solids* (Cambridge University Press, Cambridge, UK, 1993).

[25] T. Garnier, M. Nastar, P. Bellon, and D. R. Trinkle, Phys. Rev. B **88**, 134201 (2013).

[26] A. Van der Ven and G. Ceder, Phys. Rev. Lett. **94**, 045901 (2005).

[27] S. Choudhury, L. Barnard, J. Tucker, T. Allen, B. Wirth, M. Asta, and D. Morgan, J. Nucl. Mater. **411**, 1 (2011).

[28] L. Barnard, J. Tucker, S. Choudhury, T. Allen, and D. Morgan, J. Nucl. Mater. **425**, 8 (2012).

[29] A. C. Arokiam, A. V. Barashev, D. J. Bacon, and Y. N. Osetsky, Phys. Rev. B **71**, 174205 (2005).

[30] A. V. Barashev and A. C. Arokiam, Philos. Mag. Lett. **86**, 321 (2006).

[31] L. Messina, Z. Chang, and P. Olsson, Nucl. Instrum. Methods Phys. Res., Sec. B **303**, 28 (2013).

[32] M. Mantina, Y. Wang, R. Arroyave, L. Q. Chen, Z. K. Liu, and C. Wolverton, Phys. Rev. Lett. **100**, 215901 (2008).

[33] M. Mantina, Y. Wang, L. Chen, Z. Liu, and C. Wolverton, Acta Mater. **57**, 4102 (2009).

[34] J. Tucker, R. Najafabadi, T. Allen, and D. Morgan, J. Nucl. Mater. **405**, 216 (2010).

[35] L. Messina, T. Garnier, P. Olsson, and M. Nastar [Phys. Rev. B (to be published)].

[36] E. Bévillon, R. Ducher, M. Barrachin, and R. Dubourg, J. Nucl. Mater. **434**, 240 (2013).

[37] F. Soisson and C. C. Fu, Phys. Rev. B **76**, 214102 (2007).

[38] R. E. Howard and A. B. Lidiard, J. Phys. Soc. Jpn. (Suppl II) **18**, 197 (1963).

[39] J. Bocquet, Acta Metall. **22**, 1 (1974).

[40] Y. Okamura and A. R. Allnatt, J. Phys. C: Solid State Phys. **16**, 1841 (1983).

[41] M. Nastar, V. Y. Dobretsov, and G. Martin, Philos. Mag. **80**, 155 (2000).

[42] T. Anthony, *Diffusion in Solids: Recent Developments* (Academic, New York, 1975), pp. 353–378.

[43] M. Nastar, Philos. Mag. **85**, 3767 (2005).

[44] See Supplemental Material at http://link.aps.org/supplemental/10.1103/PhysRevB.89.144202 where a routine computing the Onsager matrix from a set of 16 frequencies is provided.

[45] A. R. Allnatt, J. Phys. C: Solid State Phys. **15**, 5605 (1982).

[46] A. R. Allnatt and E. L. Allnatt, Philos. Mag. A **49**(5), 625 (1984).

[47] G. Vineyard, J. Phys. Chem. Solids **3**, 121 (1957).

[48] T. Garnier, V. R. Manga, D. R. Trinkle, M. Nastar, and P. Bellon, Phys. Rev. B **88**, 134108 (2013).

[49] D. Simonovic and M. H. F. Sluiter, Phys. Rev. B **79**, 054304 (2009).

[50] G. Roma, J. Appl. Phys. **106**, 123504 (2009).

[51] C. Wolverton, Acta Mater. **55**, 5867 (2007).

[52] K. Compaan and Y. Haven, Trans. Faraday Soc. **52**, 786 (1956).

[53] G. Kuczynski, G. Matsumura, and B. Cullity, Acta Metall. **8**, 209 (1960).

[54] S. Cundy, A. Metherel, M. Whelan, P. Unwin, and R. Nicholson, Proc. R. Soc. London, Ser. A **307**, 267 (1968).

[55] T. Anthony, Acta Metall. **18**, 307 (1970).

[56] T. R. Anthony, Phys. Rev. B **2**, 264 (1970).

[57] H. Hagenschulte and T. Heumann, J. Phys.: Condens. Matter **6**, 1985 (1994).